

Systematic variations of central mass density slopes in early-type galaxies

C. Tortora^{1*}, F. La Barbera¹, N.R. Napolitano¹, A.J. Romanowsky^{2,3}, I. Ferreras⁴, R. R. de Carvalho⁵

¹ *INAF – Osservatorio Astronomico di Capodimonte, Salita Moiarriello, 16, 80131 - Napoli, Italy*

² *Department of Physics and Astronomy, San José State University, San Jose, CA 95192, USA*

³ *University of California Observatories, 1156 High Street, Santa Cruz, CA 95064, USA*

⁴ *Mullard Space Science Laboratory, University College London, Holmbury St Mary, Dorking, Surrey RH5 6NT*

⁵ *Instituto Nacional de Pesquisas Espaciais / MCTI Av. dos Astronautas 1758, Jd. Granja So José dos Campos - 12227-010 SP*

Accepted Received

ABSTRACT

We study the total density distribution in the central regions ($\lesssim 1$ effective radius, R_e) of early-type galaxies (ETGs), using data from SPIDER and ATLAS^{3D}. Our analysis extends the range of galaxy stellar mass (M_*) probed by gravitational lensing, down to $\sim 10^{10} M_\odot$. We model each galaxy with two components (dark matter halo + stars), exploring different assumptions for the dark matter (DM) halo profile (i.e. NFW, NFW-contracted, and Burkert profiles), and leaving stellar mass-to-light (M_*/L) ratios as free fitting parameters to the data. For all plausible halo models, the best-fitting M_*/L , normalized to that for a Chabrier IMF, increases systematically with galaxy size and mass. For an NFW profile, the slope of the total mass profile is non-universal, independently of several ingredients in the modeling (e.g., halo contraction, anisotropy, and rotation velocity in ETGs). For the most massive ($M_* \sim 10^{11.5} M_\odot$) or largest ($R_e \sim 15$ kpc) ETGs, the profile is isothermal in the central regions ($\sim R_e/2$), while for the low-mass ($M_* \sim 10^{10.2} M_\odot$) or smallest ($R_e \sim 0.5$ kpc) systems, the profile is steeper than isothermal, with slopes similar to those for a constant- M/L profile. For a steeper concentration-mass relation than that expected from simulations, the correlation of density slope with galaxy mass tends to flatten, while correlations with R_e and velocity dispersions are more robust. Our results clearly point to a “non-homology” in the total mass distribution of ETGs, which simulations of galaxy formation suggest may be related to a varying role of dissipation with galaxy mass.

Key words: galaxies: evolution – galaxies: general – galaxies: elliptical and lenticular, cD.

1 INTRODUCTION

In the so-called Λ CDM model, the formation of virialized dark matter (DM) haloes proceeds from the initial expansion and subsequent collapse of tiny density perturbations. The assembly and evolution of DM haloes can be studied in detail by means of N-body simulations, which predict that the DM density profile, $\rho_{\text{DM}}(r)$, should be independent of halo mass, being well described by a double power-law relation – the so-called NFW profile – with $\rho_{\text{DM}}(r) \propto r^{-3}$ in the outer regions, and $\rho_{\text{DM}}(r) \propto r^\alpha$, with $\alpha < 0$, in the centre ($\alpha = -1$, Navarro et al. 1996; $\alpha = -1.5$ Moore et al. 1998). However, N-body simulations follow only the evolution of DM parti-

cles, not including the extremely complex physics of gas and stars. These components are dominant in the central regions of galaxies, in particular those of early-type galaxies (ETGs), which exhibit a peaked surface brightness profile, typically well described by the Sérsic law (Ciotti 1991), with a shape parameter, n (Sérsic index), that accounts for variations of the light profile shape among galaxies. Gas and stars, falling down into the DM potential well, could drag a significant amount of DM particles inside, making the DM profile more concentrated in the galaxy centre (Blumenthal et al. 1986; Gnedin et al. 2004; Del Popolo 2009; Cardone et al. 2011b) than the “expected” NFW law. The study of the DM profile in the inner regions of ETGs is also hampered by the degeneracy between the shape of the DM profile and that of the

* E-mail: ctortora@na.astro.it

stellar Initial Mass Function (IMF; Napolitano et al. 2010; Dutton et al. 2011, 2012; Tortora et al. 2013).

For massive galaxies ($M_* \sim 10^{11-12} M_\odot$), gravitational lensing and studies of stellar dynamics in the galaxy central regions have found that the light and halo profiles conspire to have a total mass density profile which is nearly isothermal (Bolton et al. 2006; Bolton et al. 2008; Auger et al. 2009; Auger et al. 2010; Chae et al. 2014; Oguri et al. 2014), i.e. a total-mass density slope of $\alpha \sim -2$. The crucial questions here are why there is such a conspiracy, and if it is universal (i.e. holds for all galactic systems). Indeed, observations suggest that this is not the case. For low-mass ETGs, Dutton & Treu (2014) have recently shown that density profiles are steeper than isothermal, while they are isothermal for high-mass systems. At the mass scale of groups and clusters of galaxies, the mass density distributions appear to be also shallower than isothermal (e.g. Sand et al. 2008; Humphrey & Buote 2010). de Blok et al. (2001) also found shallower-than-isothermal profiles in low surface-brightness galaxies (with $\alpha \sim 0$). The recent theoretical work by Remus et al. (2013) seems to provide a theoretical framework to interpret these results. Their simulations show that *in-situ* star formation, resulting from dissipative processes, tends to form steeper-than-isothermal profiles, while gas-poor mergers are a natural attractor towards the isothermal slope. This motivates for further, in-depth, studies of the slope of total-mass density profiles and their correlations with galaxy properties, while making connections to the theory.

In the present work, we study the slope of the mass density profile of ETGs in a wide mass range, using data from the SDSS-based SPIDER survey (La Barbera et al. 2010), one of the largest well-characterized samples of ETGs in the nearby Universe – with high-quality spectroscopy and optical plus Near-Infrared (NIR) photometry available – as well as the ATLAS^{3D} sample (Cappellari et al. 2011). We probe the galaxy mass profiles down to a stellar mass of $10^{10} M_\odot$, hence extending, with an independent approach, results of gravitational lensing studies for massive galaxies (Bolton et al. 2006; Bolton et al. 2008; Auger et al. 2009; Auger et al. 2010). We perform a Jeans dynamical analysis of the available photometric and spectroscopic data, with a suite of dynamical models (see Tortora et al. 2013), testing several assumptions on the shape of the DM halo profile and leaving stellar mass-to-light ratios as free parameters in the analysis. Our work complements previous studies (e.g. Humphrey & Buote 2010; Dutton & Treu 2014), in that it compares findings for two independent, well-characterized, samples of ETGs, and investigates the impact of a variety of modeling ingredients. Our goal is to scrutinize if the central density slope of the total mass distribution in ETGs stays isothermal or changes with mass and other galaxy properties, comparing to predictions of simulations of galaxy formation.

The paper is organized as follows. In Sec. 2 we present the samples of ETGs used in the present study. Sec. 3 deals with data analysis, describing the dynamical modeling approach and our definitions of the mass density slope. Sec. 4 and 5 present the correlations of the mass-to-light ratio and total mass density slope with galaxy properties, i.e. structural parameters, velocity dispersion, stellar mass, and DM fraction. In Sec. 6, we present an extensive comparison of

our results with those from the literature. Sec. 7 summarizes results and conclusions.

2 SAMPLES

We rely on two samples of ETGs, one main sample from the SPIDER survey (La Barbera et al. 2010), and a complementary data-set from the ATLAS^{3D} project (Cappellari et al. 2011).

2.1 SPIDER sample

The SPIDER data-set is described in La Barbera et al. (2010). It consists of a sample of 5,080 bright ($M_r < -20$) ETGs, in the redshift range of $z = 0.05$ to 0.095 , with optical and NIR photometry available (*grizYJHK* wavebands) from the Sloan Digital Sky Survey (SDSS) DR6 and the UKIRT Infrared Deep Sky Survey-Large Area Survey DR3¹. Structural parameters, i.e. the effective radius R_e and Sérsic index n , have been measured homogeneously for all galaxies, from g through K , using the software 2DPHOT (La Barbera et al. 2008). SPIDER ETGs have central velocity dispersions, σ_{AP} , available from the SDSS, measured in the circular aperture of the SDSS fiber (having radius $R_{\text{AP}} = 1.5$ arcsec). The median ratio of the SDSS fibre to the K-band effective radius, R_{AP}/R_e , amounts to ~ 0.6 , implying only a mild extrapolation in the estimate of mass density slopes (see below).

ETGs are defined as bulge-dominated systems (i.e. SDSS parameter $\text{fracDev}_r > 0.8$, where fracDev_r measures the fraction of galaxy light better fitted by a de Vaucouleurs, rather than an exponential law), featuring passive spectra within the SDSS fibres (SDSS attribute $eClass < 0$, where $eClass$ indicates the spectral type of a galaxy based on a principal component analysis). For the present work, we rely on a subsample of ~ 4300 SPIDER ETGs, with better quality optical and NIR structural parameters, selected as in Tortora et al. (2012). For each galaxy, the stellar mass-to-light ratio, Υ_* , has been estimated by fitting Bruzual & Charlot (2003) stellar population models to the multi-band photometry, under the assumption of a Chabrier IMF (see Swindle et al. (2011) and Tortora et al. (2012) for details). The sample is 95% complete down to a stellar mass of $M_* \sim 3 \times 10^{10} M_\odot$.

2.2 ATLAS^{3D} sample

Our second sample consists of 260 ETGs from the ATLAS^{3D} survey (Cappellari et al. 2013b,a). Further details about the selection of ATLAS^{3D} galaxies are provided in Tortora et al. (2014). For each galaxy, we perform the dynamical analysis by using (i) its r -band effective radius, R_e , (ii) the r -band total luminosity L_r , (iii) the projected stellar velocity dispersion, σ_e , within R_e , and (iv) the stellar mass-to-light ratio (Υ_*) derived by fitting galaxy spectra with Vazdekis et al. (2012) single SSP MILES models, having a Salpeter (1955) IMF. Stellar masses are converted to a Chabrier (2001) IMF, using the fact that the Chabrier IMF normalization is ~ 0.26

¹ <http://www.sdss.org>, <http://www.ukidss.org>

dex smaller than the Salpeter one. We notice that out of 260 ETGs, about 15% of ATLAS^{3D} ETGs have significant stellar mass-to-light ratio gradients and young stellar populations (with an H β equivalent width $>2.3 \text{ \AA}$). We found that excluding these objects from the analysis does not affect at all the trends of total-mass density slope.

As discussed in Tortora et al. (2014), it is important to note that the published L_r and R_e values are not self-consistent. The former correspond to detailed multi-gaussian expansion (MGE) fits that were truncated at typically $\sim 4 R_e$. The latter are the MGE-based values renormalized by a factor of 1.35 to correspond to more conventional estimates from the literature. Here we will use these R_e values, but adjust each L_r value such that the projected luminosity inside R_e for our adopted de Vaucouleurs model is the same as in the original MGE model. This means increasing L_r by typically a factor of 1.2.

3 ANALYSIS

3.1 Dynamical modeling

We derive the dynamical (i.e. total) mass distribution of ETGs by solving spherical isotropic Jeans equations, where a given model for the mass profile is fitted to σ_{Ap} and σ_e , for SPIDER and ATLAS^{3D} ETGs, respectively. We use two-component mass models, describing stars and DM.

The stellar mass profile is modeled by either a Sérsic (SPIDER) or a de Vaucouleurs (1948) (ATLAS^{3D}) law. The shape parameter n and effective radius of the Sérsic laws are those obtained by fitting galaxy images in K band (see Sec. 2). For the de Vaucouleurs law, we use r-band effective radii from the ATLAS^{3D} sample. In both cases, the total luminosity of the light distribution is converted into stellar mass by means of the stellar mass-to-light ratio, Υ_* , which is a free fitting parameter². This procedure assumes that the shape and scale radius of the stellar mass distribution of ETGs are the same as for the light distribution, i.e. one can neglect Υ_* gradients inside these galaxies. One can notice that although Sérsic fits are known to provide a better fit to the light distribution of ETGs than a pure de Vaucouleurs law, a comparison of results for Sérsic (SPIDER) vs. de Vaucouleurs (ATLAS^{3D}) profiles is useful to test the robustness of the results against the parametrization of the galaxy light distribution. Also, K-band light is more sensitive to the old quiescent component of an unresolved stellar population, describing more closely the stellar mass profile of a galaxy, than the light distribution at optical wavebands. Hence, the comparison of K- (SPIDER) and r- (ATLAS^{3D}) band results allows us to test the impact of stellar mass-to-light ratio gradients in galaxies, besides that of selecting two different samples of ETGs, and using different parametrizations of the galaxy light profiles. As a further test, we also compare

² Note that stellar mass-to-light ratios estimated from stellar population models (Sec. 2) are not used to derive the density slopes, but only as reference values to normalize the best-fitting Υ_* s, and to produce correlations of density slope with stellar-mass estimates for a “standard” (i.e. MW-like) IMF (allowing a more direct comparison to other studies).

our findings to those obtained for the (same) SPIDER sample using (SDSS-based) de Vaucouleurs (rather than Sérsic) structural parameters in the r (rather than K) band. In general, as discussed below, assuming a constant Υ_* does not likely affect significantly our conclusions.

For the DM component, in the case of the SDSS-based SPIDER sample we can rely only on velocity dispersions measured within a single aperture (i.e. the SDSS fibre), which does not allow us to constrain the shape of the DM profile in detail. In contrast, using the spatially extended kinematics of ATLAS^{3D} galaxies, one could constrain, in principle, the shape of both the stellar and DM components in the central galaxy regions in detail, as shown, e.g., in Cappellari et al. (2012). In the present work, to perform a clean comparison of results from both samples, we apply the same procedure to both SPIDER and ATLAS^{3D} ETGs, fitting two-component models to central velocity dispersion estimates for both samples. To this effect, we explore a variety of models for the DM component, exploring several plausible assumptions (Tortora et al. 2013).

Navarro et al. (1996, hereafter NFW) profiles. The DM profile from N-body simulations is well described by a double power-law, commonly referred to as the NFW profile (Navarro et al. 1996, 1997). In the present work, we adopt the NFW as the reference DM profile, assuming also the correlation between virial mass and concentration (M_{vir} and c_{vir} , respectively), that applies to a WMAP5 cosmology (Macciò et al. 2008) as well as the $M_{\text{vir}}-M_*$ ^{Chab} correlation from Moster et al. (2010). In order to explore the effect of a possible modification to the DM profile because of the interaction between gas and stars with DM, we also consider the case of an NFW with an adjustable degree of baryon-induced adiabatic contraction (AC, Gnedin et al. 2004). Also, we explore how our results depend on the assumed $M_{\text{vir}}-c_{\text{vir}}$ relation, by (i) adopting a constant $M_{\text{vir}}=10^{13} M_{\odot}$ (and deriving the corresponding, constant, c_{vir} from the Macciò et al. 2008 $M_{\text{vir}}-c_{\text{vir}}$ relation), and (ii) using the $c_{\text{vir}}-M_{\text{vir}}$ correlation, based on observations, from Leier et al. (2012, hereafter LFS12). In the latter case, we adopt the relation obtained from LFS12 by combining X-ray results from Buote et al. (2007) with a gravitational lensing analysis of galaxies at intermediate redshifts³. For the median redshift of the SPIDER sample ($z \sim 0.08$), the relation is written as $c_{\text{vir}} = 9.62 \times M_{\text{vir}}^{-0.278}$. Notice that although LFS12 found some evidence for a variation of the slope of the $M_{\text{vir}}-c_{\text{vir}}$ relation with the M_{vir} range fitted, this is unimportant for the relatively narrow mass range covered by our sample of ETGs with respect to that of LFS12. As discussed below, the LFS12 relation is significantly steeper than the Macciò et al. (2008) one, providing significantly higher concentrations for the lowest mass galaxies analyzed in this work. Also, LFS12 assumed a MW-like, Chabrier, IMF to map the stellar mass distribution of lensing galaxies, while in the present study we keep the Υ_* (i.e. the “IMF normalization”) as a free fitting parameter. In the following, we refer to models with NFW profiles and a $c_{\text{vir}}-M_{\text{vir}}$ relation from LFS12 as “high-concentration” NFW models.

³ We used the Eq. (11) from LFS12, with the *comb* best-fitting slope and normalization coefficients from their Table 1.

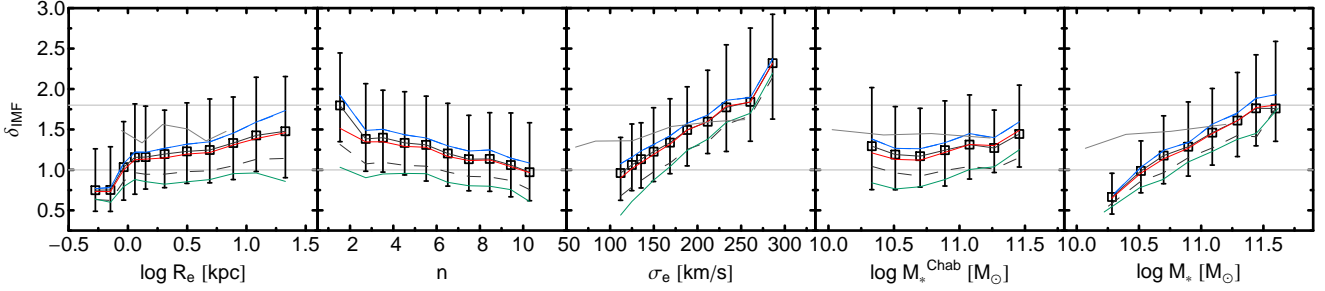


Figure 1. IMF mismatch parameter, δ_{IMF} , for our sample of SPIDER ETGs, as a function of (from left to right) R_e , n , σ_e , M_*^{Chab} (estimated for a Chabrier IMF) and M_* (allowing for a variable IMF normalization). Open squares and error bars are median and 16–84th percentile trends for our fiducial NFW+Sérsic galaxy model. We also plot results for NFW models with fixed $M_{\text{vir}} = 10^{13} M_{\text{vir}}$ (red curve), “high-concentration” NFW models (dashed black line), and Burkert profiles with $r_B = 1$ kpc (solid blue line). Notice that results for Burkert models with $r_B = 20$ kpc are not shown in the plot, as the corresponding trends are identical to the case for $r_B = 1$ kpc. The results for ATLAS^{3D} using the fiducial NFW+Sérsic galaxy model are plotted as dark gray lines. Light gray horizontal lines mark the δ_{IMF} values expected for a Chabrier ($\delta_{\text{IMF}} = 1$) and Salpeter ($\delta_{\text{IMF}} \sim 1.8$) IMF.

Burkert (1995) profiles. The Burkert profile is the prototype of cored models, and has been shown to reproduce quite well the DM profile of spirals and dwarf galaxies. The density and scale parameter of the Burkert profile (ρ_B and r_B , respectively) are assumed to follow the $\rho_B - r_B$ relation from Salucci & Burkert (2000), adjusted to match results at higher surface density, for two ETGs, by Memola et al. (2011, hereafter MSB11). We explore two cases in detail, where the scale radius is set to $r_B = 1$ and 20 kpc, respectively. The possible impact of a varying r_B (with, e.g., galaxy mass) on our results is discussed in Sec. 5.2.

For each galaxy and a given DM model, one has one single fitting parameter, i.e. the mass-to-light ratio Υ_* . The Υ_* is constrained by solving the Jeans equations to match the available velocity dispersion estimate (see above). We have performed several tests, showing that our results are quite independent of the assumptions on the DM profile. None of the conclusions is changed when comparing results for NFW profiles with either a constant $M_{\text{vir}} = 10^{13} M_{\odot}$ (and constant c_{vir}), or the Macciò et al. (2008) $c_{\text{vir}} - M_{\text{vir}}$ relation. However, assuming a cored Burkert profile or high concentration haloes – consistent with LFS12 – can affect significantly some of our results, as discussed below.

3.2 Inferring the slope of the density profile

We aim here to study the slope of the total mass profile of ETGs, rather than that of DM only (as in our previous work, see Napolitano et al. 2010). For each galaxy, at a given (deprojected) galacto-centric distance, r , the total mass density, $\rho(r)$, is obtained by summing the best-fitting stellar mass profile and the DM profile at that radius. In order to probe the robustness of the correlations between mass-density slope and galaxy properties, we adopt different definitions of the slope.

- i) We define the local logarithmic slope of the profile, $\alpha_1(r) = d \log \rho(r) / d \log r$;
- ii) We compute the *mass-weighted logarithmic slope*, α_{mw} , within a given radius r (Koopmans et al. 2009; Dutton & Treu 2014). It is defined as:

$$\alpha_{\text{mw}}(r) \equiv \frac{1}{M(r)} \int_0^r \alpha_1(r) 4\pi x^2 \rho(x) dx = -3 + \frac{4\pi r^3 \rho(r)}{M(r)}, \quad (1)$$

where $M(r)$ is the (total) mass enclosed within a sphere of radius r . Some algebra shows that

$$\alpha_{\text{mw}}(r) = -3 + d \log M(r) / d \log r. \quad (2)$$

For a power-law density profile, $\rho \propto r^\alpha$, one has $\alpha_1(r) = \alpha_{\text{mw}}(r) = \alpha$ at all radii, while this is not true for a general density distribution. However, in general, one can demonstrate that $\alpha_{\text{mw}}(r) > \alpha$. We calculate the logarithmic slope at two different radii, i.e. $R_e/2$ and R_e , respectively, while the mass-weighted slope is computed within $r = R_e$. These choices are motivated by the fact that the available estimates of velocity dispersion refer to an aperture with radius ranging from a few tenths of R_e to about one R_e , for both the SPIDER and ATLAS^{3D} samples. Thus, our choice minimizes the amount of extrapolation of the best-fitting mass models, exploring at the same time the inner profile at different radii ($R_e/2$ and R_e).

In the following sections we will discuss these slopes in terms of R_e , Sérsic n , σ_e , stellar mass and central DM fraction within a radius R , defined as $f_{\text{DM}}(R) = 1 - M_*(R)/M_{\text{tot}}(R)$.

4 MASS-TO-LIGHT RATIO TRENDS

Using the dynamical estimate of Υ_* (see Sec. 3), we define the mismatch parameter, $\delta_{\text{IMF}} = \Upsilon_*/\Upsilon_*^{\text{Chab}}$, where Υ_*^{Chab} is the stellar mass-to-light ratio obtained by fitting data (either colors or galaxy spectra) with stellar population models having a Chabrier IMF. The δ_{IMF} can be interpreted as a variation in the normalization of the IMF with respect to the case of a “standard”, Milky-Way-like, distribution.

Fig. 1 plots the mismatch parameter as a function of R_e , Sérsic index n , σ_e and M_* , the latter estimated with either Υ_*^{Chab} (i.e. a Chabrier IMF; M_*^{Chab}) or Υ_* (i.e., the best-fitting IMF normalization; M_*). We find that δ_{IMF} is positively correlated with R_e , σ_e , and M_* , becoming larger than 1 in more massive and bigger galaxies. In contrast, the δ_{IMF} decreases with n , while it is almost constant with M_*^{Chab} . The trends for Burkert and “high-concentration” NFW models encompass the range of values for all trends.

Although the absolute value of δ_{IMF} depends on the adopted DM profile in the modeling, the relative trends of δ_{IMF} trends with galaxy parameters are robust, being independent of the assumptions on the DM model (e.g., NFW vs. AC+NFW vs. Burkert profiles), and the assumed $c_{\text{vir}} - M_{\text{vir}}$ relation.

The mismatch parameter for ATLAS^{3D} using the fiducial NFW+Sérsic galaxy model is also shown. All the correlations are shallower, and Υ_* have values $\sim 15\%$ larger than SPIDER-based results (e.g. Tortora et al. 2013).

As noted by Cappellari et al. (2012), a δ_{IMF} larger than one can be due to either a bottom-heavy IMF (because of the large fraction of dwarf relative to giant stars) or a top-heavy distribution (because of the large fraction of stellar remnants from evolved massive stars). The degeneracy can be broken by studying gravity-sensitive features in the integrated light of ETGs (Conroy & van Dokkum 2012). These features allow one to constrain the mass fraction of dwarf-to-giant stars in the IMF, rather than the IMF normalization itself (La Barbera et al. 2013), with several studies having found evidence for a bottom-heavier than Chabrier IMF, in high- relative to low- σ ETGs (Ferrerias et al. 2013; Spiniello et al. 2014). As shown in Fig. 1, at large R_e and σ_e , our results are consistent with the IMF normalization expected for a Salpeter IMF, or even a bottom-heavier than Salpeter IMF.

These results extend our previous analysis in Tortora et al. (2013), in that we explore here a larger set of DM models (i.e. Burkert and “high-concentration” NFW models), and present also the correlations of δ_{IMF} with R_e , n , and mass (besides that with σ), and are consistent with a plethora of independent results from dynamical and stellar population studies (Treu et al. 2010; Thomas et al. 2011; Conroy & van Dokkum 2012; Cappellari et al. 2012, 2013a; Spiniello et al. 2012; Wegner et al. 2012; Dutton et al. 2013; Ferreras et al. 2013; Goudfrooij & Kruijssen 2013; La Barbera et al. 2013; Tortora et al. 2013; Weidner et al. 2013; Tortora et al. 2014; Goudfrooij & Kruijssen 2014; Shu et al. 2014). We notice that for “high-concentration” NFW models the best-fitting Υ_* is significantly lower (by ~ 0.5 dex, at $\sigma_e \sim 100 \text{ km s}^{-1}$) than that for a Chabrier IMF (i.e. $\delta_{\text{IMF}} < 1$). Since the Chabrier IMF gives a minimum normalization with respect to either top- or bottom-heavier distributions (see above), our data seem to be more consistent with a somewhat lower concentration than that of the LFS12 $c_{\text{vir}} - M_{\text{vir}}$ relation (see Section 3), although measurement uncertainties on c_{vir} and Υ_*^{Chab} might indeed be responsible for the low (< 1) δ_{IMF} values.

5 TOTAL MASS DENSITY SLOPES

5.1 Correlations with galaxy properties

We start by presenting results for the SPIDER sample, where the stellar mass profiles of ETGs are characterized with Sérsic fits of NIR (K-band) galaxy images (see Sec. 2.1). In this section, we focus the discussion on results for our reference NFW model, comparing those for different models in Section 5.2. Fig. 2 shows the correlations of logarithmic mass slopes, $\alpha_1(R_e/2)$ (top) and $\alpha_1(R_e)$ (bottom), as a function of R_e , Sérsic n , σ_e , and stellar mass (using either a

Chabrier IMF, or the IMF normalization provided by our best-fit model for each galaxy). The σ_e is the SDSS-fibre velocity dispersion, σ_{Ap} , corrected to an aperture of one R_e , following Cappellari et al. (2006). Fig. 3 shows the same correlations as in Fig. 2 but for the mass-weighted (rather than local) slope, $\alpha_{\text{mw}}(R_e)$. Comparing the Figures, one can see that the slope value depends significantly on its definition, i.e. $\alpha_1(R_e/2) \neq \alpha_1(R_e) \neq \alpha_{\text{mw}}(R_e)$ within the uncertainties, suggesting that either the total mass profile of ETGs is not exactly a power-law, or the explored set of models – which are non-power-laws by construction – is not able to describe accurately a power-law behavior of the profiles (see Sec. 3.2). More (spatially extended) kinematical data would be necessary to address this issue.

In Tables 1, 2 and 3 we show the results of fitting the trends in Figs. 2 and 3, with 2nd order polynomials of the form $\alpha = a + bx + cx^2$. Errors on slopes are computed by a bootstrap method, and are quoted at the 1σ level. Almost all the correlations are significant at more than 99%.

For our reference, NFW, DM models (solid black curves in the Figures), the α_1 becomes shallower with galaxy mass and radius, reaching, for the highest radii probed, a value of about -1.5 , i.e. even shallower than the isothermal value (-2). Milder trends of α_1 , than those for R_e and mass, are observed with respect to Sérsic n and σ_e . At $R_e/2$, the α_1 exhibits a double-value behaviour as a function of n , increasing at both high and low n , while $\alpha_1(R_e)$ tends to steepen with n . In terms of σ_e , both $\alpha_1(R_e/2)$ and $\alpha_1(R_e)$ tend to steepen with velocity dispersion. For $\alpha_{\text{mw}}(R_e)$, as it might be expected, the trends are intermediate between those for $\alpha_1(R_e/2)$ and $\alpha_1(R_e)$. In general, $\alpha_{\text{mw}}(R_e)$ increases with mass and radius, while it exhibits a double-value behavior with n , and mildly decreases with σ_e , consistent with the findings for $\alpha_1(R_e/2)$ and $\alpha_1(R_e)$.

Figs. 2 and 3 also plot the slopes of the stellar mass profile only (shaded regions), obtained from the best-fitting K-band Sérsic profiles, under the assumption of a radially-constant (stellar) M/L (see Sec. 3). In contrast to α_1 , the stellar mass slope does not vary significantly with R_e and M_* . No significant variation with σ_e is observed (similar to α_1), while the stellar mass slope tends to steepen with n , as expected by the fact that as n increases the shape of the Sérsic law becomes more peaked towards the centre. Interestingly, at low R_e and M_* , the NFW-based total mass density slope approaches the slope of the stellar mass component, i.e. that for a constant- M/L profile. This is due to the fact that in the centre of low-mass (small) ETGs, the stellar mass distribution dominates the total mass budget. Notice that Tortora et al. (2009b) reached a similar conclusion by comparing central DM density estimates with predictions of Λ CDM toy-models.

For the ATLAS^{3D} sample, we get, in general, consistent results with those for the SPIDER sample. Fig. 4 (left-panel) compares, for example, the trends of $\alpha_1(R_e)$ with M_* for both samples. The best fit trend for SPIDER shown in Table 2 is $\alpha_1(R_e) = -1.88 + 0.87M_* - 0.04M_*^2$ with scatter of $rms = 0.303$, while for ATLAS^{3D} we find $\alpha_1(R_e) = -2.23 + 0.68M_* + 0.69M_*^2$ and a scatter of $rms = 0.207$. We remark that SPIDER and ATLAS^{3D} ETGs are analyzed here with the same approach, although the galaxy light distributions and stellar masses are characterized in significantly different ways. In fact, the $n = 4$ light pro-

Table 1. Best fit parameters with 1σ errors for the relation $\alpha_1(R_e/2) = a + bx + cx^2$, where $x = \log R_e/3\text{kpc}$, $n/4$, $\sigma_e/200\text{km/s}$, $\log M_\star^{\text{Chab}}/(10^{11}M_\odot)$ and $\log M_\star/(10^{11}M_\odot)$. The scatter (rms) around the best fit relation is also reported.

Model		Best fit				
		$\alpha - R_e$	$\alpha - n$	$\alpha - \sigma_e$	$\alpha - M_\star^{\text{Chab}}$	$\alpha - M_\star$
NFW+light	a	-2.288 ± 0.005	-1.28 ± 0.06	-1.66 ± 0.13	-2.14 ± 0.01	-2.23 ± 0.01
	b	0.65 ± 0.01	-1.54 ± 0.08	-1.13 ± 0.32	0.63 ± 0.06	0.35 ± 0.03
	c	0.33 ± 0.02	0.54 ± 0.03	0.42 ± 0.18	0.35 ± 0.09	0.13 ± 0.05
	rms	0.148	0.261	0.274	0.255	0.274
NFW ($M_{\text{vir}} = 10^{13} M_\odot$)	a	-2.20 ± 0.01	-1.29 ± 0.04	-1.11 ± 0.10	-2.12 ± 0.01	-2.17 ± 0.01
	b	0.64 ± 0.01	-1.48 ± 0.07	-1.97 ± 0.24	0.21 ± 0.04	0.11 ± 0.02
	c	0.17 ± 0.02	0.53 ± 0.02	0.73 ± 0.13	-0.10 ± 0.08	-0.03 ± 0.05
	rms	0.192	0.263	0.241	0.293	0.301
NFW+AC	a	-2.19 ± 0.01	-1.43 ± 0.03	-1.62 ± 0.10	-2.07 ± 0.01	-2.14 ± 0.01
	b	0.51 ± 0.01	-1.11 ± 0.06	-0.96 ± 0.23	0.47 ± 0.03	0.25 ± 0.03
	c	0.22 ± 0.02	0.38 ± 0.02	0.31 ± 0.13	0.25 ± 0.07	0.26 ± 0.05
	rms	0.138	0.217	0.214	0.205	0.226
Burkert ($r_B = 20$ kpc)	a	-2.59 ± 0.01	-1.29 ± 0.04	-2.34 ± 0.08	-2.54 ± 0.005	-2.539 ± 0.004
	b	0.24 ± 0.01	-1.57 ± 0.06	-0.43 ± 0.19	0.13 ± 0.02	0.13 ± 0.01
	c	0.36 ± 0.03	0.44 ± 0.02	0.18 ± 0.11	0.13 ± 0.05	-0.05 ± 0.02
	rms	0.164	0.170	0.192	0.197	0.195
Burkert ($r_B = 1$ kpc)	a	-2.615 ± 0.004	-1.42 ± 0.04	-2.73 ± 0.12	-2.688 ± 0.005	-2.652 ± 0.004
	b	-0.10 ± 0.01	-1.27 ± 0.05	0.12 ± 0.28	-0.06 ± 0.02	-0.03 ± 0.01
	c	-0.12 ± 0.02	0.30 ± 0.02	-0.03 ± 0.15	0.16 ± 0.04	-0.04 ± 0.02
	rms	0.152	0.055	0.155	0.152	0.158
NFW (LFS $c_{\text{vir}} - M_{\text{vir}}$)	a	-1.776 ± 0.005	-1.51 ± 0.03	-0.89 ± 0.17	-1.68 ± 0.01	-1.8 ± 0.01
	b	0.55 ± 0.02	-0.51 ± 0.05	-1.48 ± 0.40	0.32 ± 0.05	0.08 ± 0.02
	c	-0.35 ± 0.03	0.19 ± 0.02	0.40 ± 0.22	0.02 ± 0.09	0.29 ± 0.04
	rms	0.190	0.239	0.200	0.243	0.253
Sérsic light	a	-2.624 ± 0.005	-1.43 ± 0.04	-2.78 ± 0.09	-2.692 ± 0.005	-2.66 ± 0.01
	b	-0.09 ± 0.01	-1.27 ± 0.05	0.19 ± 0.23	-0.05 ± 0.02	-0.01 ± 0.01
	c	-0.11 ± 0.02	0.3 ± 0.02	-0.06 ± 0.13	0.15 ± 0.04	-0.05 ± 0.02
	rms	0.141	0.055	0.158	0.152	0.158

Table 2. Best fit parameters with 1σ errors for the relation $\alpha_1(R_e) = a + bx + cx^2$, where $x = \log R_e/3\text{kpc}$, $n/4$, $\sigma_e/200\text{km/s}$, $\log M_\star^{\text{Chab}}/(10^{11}M_\odot)$ and $\log M_\star/(10^{11}M_\odot)$. The scatter (rms) around the best fit relation is also reported.

Model		Best fit				
		$\alpha - R_e$	$\alpha - n$	$\alpha - \sigma_e$	$\alpha - M_\star^{\text{Chab}}$	$\alpha - M_\star$
NFW+light	a	-2.141 ± 0.005	-2.33 ± 0.03	-1.02 ± 0.24	-1.88 ± 0.02	-2.06 ± 0.01
	b	0.86 ± 0.01	-0.21 ± 0.05	-2.05 ± 0.54	0.87 ± 0.03	0.57 ± 0.02
	c	-0.03 ± 0.02	0.2 ± 0.01	0.75 ± 0.30	-0.04 ± 0.07	0.23 ± 0.07
	rms	0.170	0.292	0.341	0.303	0.339
NFW ($M_{\text{vir}} = 10^{13} M_\odot$)	a	-1.97 ± 0.01	-2.34 ± 0.04	-0.28 ± 0.18	-1.82 ± 0.02	-1.93 ± 0.02
	b	0.81 ± 0.01	-0.01 ± 0.05	-3.04 ± 0.43	0.21 ± 0.04	0.14 ± 0.03
	c	-0.31 ± 0.02	0.14 ± 0.02	1.07 ± 0.23	-0.68 ± 0.13	-0.08 ± 0.09
	rms	0.224	0.285	0.292	0.348	0.359
NFW+AC	a	-2.11 ± 0.01	-2.29 ± 0.03	-1.37 ± 0.13	-1.90 ± 0.01	-2.03 ± 0.01
	b	0.64 ± 0.01	-0.07 ± 0.04	-1.29 ± 0.31	0.68 ± 0.03	0.43 ± 0.02
	c	0.04 ± 0.03	0.12 ± 0.02	0.42 ± 0.16	0.05 ± 0.07	0.37 ± 0.05
	rms	0.158	0.241	0.268	0.237	0.272
Burkert ($r_B = 20$ kpc)	a	-2.6 ± 0.01	-2.05 ± 0.03	-2.10 ± 0.09	-2.55 ± 0.01	-2.61 ± 0.01
	b	0.56 ± 0.01	-1.12 ± 0.05	-1.03 ± 0.21	0.28 ± 0.02	0.26 ± 0.02
	c	0.25 ± 0.03	0.44 ± 0.02	0.41 ± 0.10	-0.09 ± 0.05	-0.01 ± 0.04
	rms	0.205	0.265	0.305	0.311	0.321
Burkert ($r_B = 1$ kpc)	a	-2.832 ± 0.001	-2.24 ± 0.02	-2.87 ± 0.05	-2.868 ± 0.002	-2.854 ± 0.001
	b	-0.062 ± 0.003	-0.64 ± 0.03	0.03 ± 0.11	-0.04 ± 0.01	-0.029 ± 0.005
	c	-0.037 ± 0.005	0.15 ± 0.01	-0.01 ± 0.06	0.09 ± 0.02	0.02 ± 0.01
	rms	0.063	0.032	0.071	0.071	0.071
NFW (LFS $c_{\text{vir}} - M_{\text{vir}}$)	a	-1.716 ± 0.007	-2.1 ± 0.04	-1.64 ± 0.27	-1.673 ± 0.005	-1.76 ± 0.01
	b	0.32 ± 0.02	0.38 ± 0.06	-0.04 ± 0.66	0.38 ± 0.02	0.19 ± 0.02
	c	-0.5 ± 0.04	-0.09 ± 0.02	-0.22 ± 0.38	0.21 ± 0.05	0.34 ± 0.03
	rms	0.173	0.195	0.192	0.184	0.214
Sérsic light	a	-2.841 ± 0.002	-2.25 ± 0.02	-2.91 ± 0.05	-2.871 ± 0.002	-2.856 ± 0.002
	b	-0.041 ± 0.005	-0.64 ± 0.03	0.08 ± 0.11	-0.02 ± 0.01	-0.01 ± 0.01
	c	-0.05 ± 0.01	0.15 ± 0.01	-0.02 ± 0.06	0.066 ± 0.02	-0.02 ± 0.01
	rms	0.063	0.032	0.071	0.071	0.071

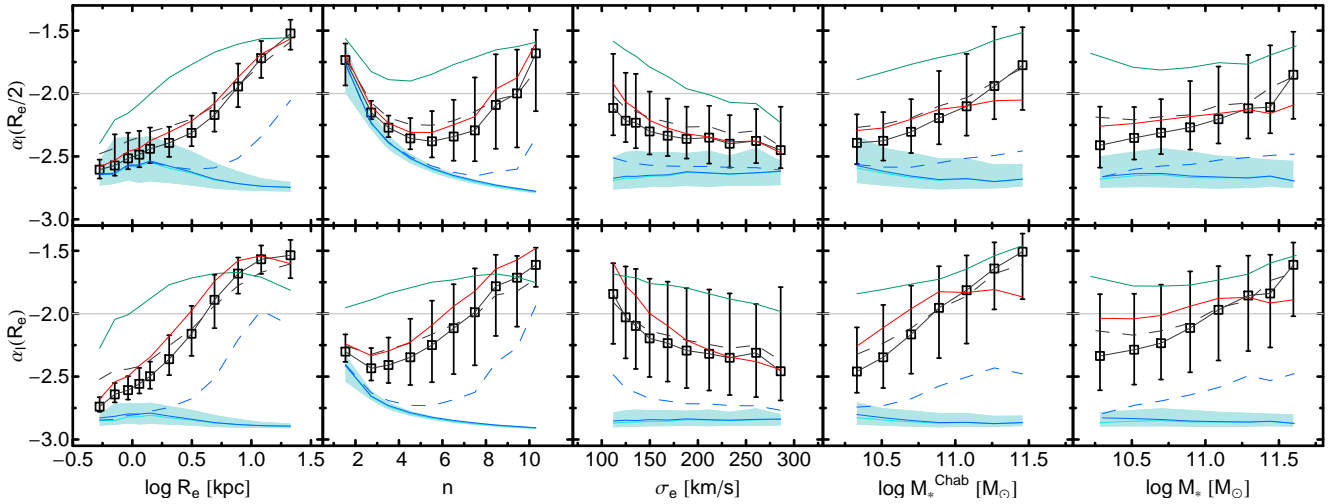


Figure 2. Mass density slopes, for our sample of SPIDER ETGs, as a function of (from left to right) R_e , n , σ_e , M_*^{Chab} (Chabrier-IMF stellar mass) and M_* (stellar mass estimated allowing for a variable IMF normalization). Top and bottom panels refer to the logarithmic slopes, $\alpha_1(R_e/2)$ and $\alpha_1(R_e)$, respectively. All slope values are for models with variable Υ_* . Symbols are as in Fig. 1. Results for Burkert profile with $r_B = 1$ and 20 kpc are plotted as solid blue and dashed blue lines, respectively. The cyan line and shaded regions mark median and 16–84th percentile slopes for the stellar mass distribution only. In all panels, the gray horizontal line marks the slope value of -2 , corresponding to the case of an isothermal sphere.

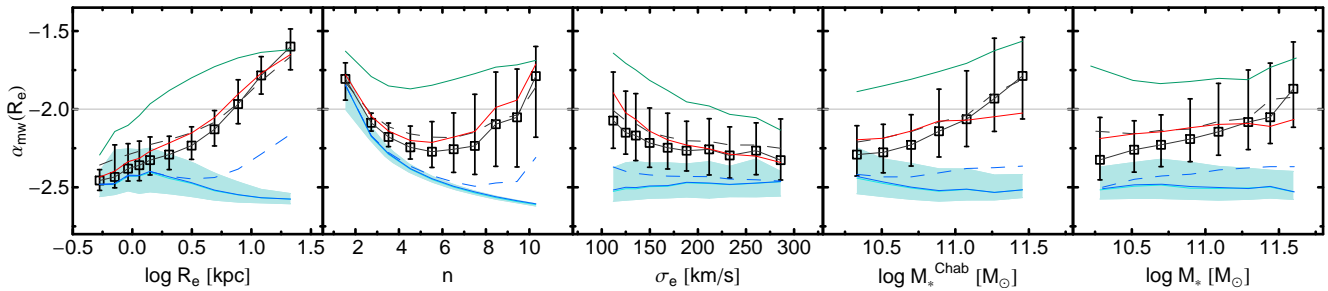


Figure 3. The same as Fig. 2, but for the mass-weighted density slope $\alpha_{\text{mw}}(R_e)$.

files for ATLAS^{3D} galaxies have shallower slopes with respect to the SPIDER Sérsic laws⁴. The agreement between the two data-sets is good, although the trend with mass for ATLAS^{3D} tends to be shallower than that for SPIDER, with steeper slopes at high masses, because of the shallower (de Vaucouleurs vs. Sérsic) light profile. At the lowest M_* ($\sim 10^{10} M_\odot$), which can be probed only with ATLAS^{3D}, one can observe an inversion of the mass density trend with the slope, with α_1 becoming shallower than at $M_* \sim 10^{10.5} M_\odot$. However, this result might be just reflecting the fact that the $r^{1/4}$ law is not very accurate for low, relative to high, mass ETGs. The right panel of Fig. 4 also shows the correlation of mass density slopes with central DM fraction within R_e , $f_{\text{DM}}(R_e)$. As for best fits in Tables 1, 2 and 3, the trend is quite well fitted by a polynomial. We find $\alpha_1(R_e) = -2.65 + 3.42x - 2.52x^2$, with $x = f_{\text{DM}}(R_e)$ and a scatter of 0.07. For ATLAS^{3D} the fit is $\alpha_1(R_e) = -2.73 + 3.91x - 3.94x^2$ with the same scatter

⁴ Cappellari et al. (2013b) found that stellar light profiles were well fitted by an isothermal law within 1 R_e (see their Fig. 2). Our stellar-light slopes for the ATLAS^{3D} galaxies would be consistent with their findings if the same slope definition were adopted.

found for SPIDER sample. We find consistent results between the two data-sets, with shallower density profiles in galaxies that are more DM dominated in the center, consistent with independent results from Auger et al. (2010) and Dutton & Treu (2014) (see below).

Fig. 4 also compares the SPIDER and ATLAS^{3D} trends with those obtained for SPIDER ETGs, by computing density mass slopes and dark matter fractions with $r^{1/4}$ (i.e. de Vaucouleurs) structural parameters in r band from SDSS-DR6, rather than Sérsic 2DPHOT parameters in K band (see La Barbera et al. (2010) for details). This comparison allows us to single out the effect of differences due to light profile shape, from those of different wavebands and sample selection, on the observed trends. The $r^{1/4}$ trends with M_* are shallower than reference ones for SPIDER, and fairly consistent with those for ATLAS^{3D}, the small difference between solid (ATLAS^{3D}) and dashed (SPIDER $r^{1/4}$) gray curves being likely explained by differences in sample selection. The fact that $r^{1/4}$, with respect to Sérsic, parameters provide steeper density slopes is also consistent with the trends in the bottom panels of Fig. 2. In fact, fitting a $n = 4$ light profile gives smaller R_e values than those for a Sérsic

Table 3. Best fit parameters with 1σ errors for the relation $\alpha_{\text{mw}}(R_e) = a + bx + cx^2$, where $x = \log R_e/3\text{kpc}$, $n/4$, $\sigma_e/200\text{km/s}$, $\log M_\star^{\text{Chab}}/(10^{11} M_\odot)$ and $\log M_\star/(10^{11} M_\odot)$. The rms is also reported. The scatter (rms) around the best fit relation is also reported.

Model		Best fit				
		$\alpha - R_e$	$\alpha - n$	$\alpha - \sigma_e$	$\alpha - M_\star^{\text{Chab}}$	$\alpha - M_\star$
NFW	a	-2.218 ± 0.004	-1.47 ± 0.04	-1.73 ± 0.09	-2.1 ± 0.01	-2.16 ± 0.01
	b	0.50 ± 0.01	-1.12 ± 0.06	-0.85 ± 0.2	0.51 ± 0.3	0.28 ± 0.02
	c	0.28 ± 0.01	0.38 ± 0.02	0.31 ± 0.10	0.35 ± 0.06	0.09 ± 0.04
	rms	0.122	0.212	0.212	0.195	0.210
NFW ($M_{\text{vir}} = 10^{13} M_\odot$)	a	-2.139 ± 0.005	-1.45 ± 0.04	-1.24 ± 0.09	-2.08 ± 0.01	-2.11 ± 0.01
	b	0.48 ± 0.01	-1.08 ± 0.06	-1.62 ± 0.19	0.14 ± 0.03	0.07 ± 0.02
	c	0.13 ± 0.02	0.38 ± 0.02	0.61 ± 0.10	-0.08 ± 0.06	-0.07 ± 0.04
	rms	0.161	0.217	0.184	0.235	0.239
NFW+AC	a	-2.147 ± 0.005	-1.57 ± 0.03	-1.62 ± 0.13	-2.05 ± 0.01	-2.11 ± 0.01
	b	0.40 ± 0.01	-0.83 ± 0.04	-0.93 ± 0.32	0.41 ± 0.04	0.21 ± 0.02
	c	0.20 ± 0.02	0.27 ± 0.01	0.35 ± 0.18	0.25 ± 0.08	0.23 ± 0.03
	rms	0.130	0.190	0.184	0.176	0.192
Burkert ($r_B = 20$ kpc)	a	-2.431 ± 0.004	-1.51 ± 0.02	-2.25 ± 0.08	-2.401 ± 0.004	-2.398 ± 0.004
	b	0.13 ± 0.01	-1.1 ± 0.04	-0.31 ± 0.19	0.07 ± 0.01	0.09 ± 0.01
	c	0.16 ± 0.02	0.30 ± 0.01	0.13 ± 0.11	0.05 ± 0.03	-0.07 ± 0.01
	rms	0.122	0.105	0.130	0.134	0.134
Burkert ($r_B = 1$ kpc)	a	-2.463 ± 0.004	-1.58 ± 0.02	-2.58 ± 0.09	-2.524 ± 0.004	-2.49 ± 0.01
	b	-0.09 ± 0.01	-0.92 ± 0.03	0.17 ± 0.22	-0.05 ± 0.02	-0.02 ± 0.01
	c	-0.1 ± 0.01	0.21 ± 0.01	-0.05 ± 0.13	0.14 ± 0.04	-0.05 ± 0.02
	rms	0.110	0.032	0.126	0.118	0.126
NFW (LFS $c_{\text{vir}} - M_{\text{vir}}$)	a	-1.804 ± 0.004	-1.55 ± 0.03	-1.06 ± 0.12	-1.72 ± 0.01	-1.83 ± 0.01
	b	0.44 ± 0.01	-0.42 ± 0.04	-1.29 ± 0.28	0.29 ± 0.04	0.08 ± 0.02
	c	-0.27 ± 0.02	0.15 ± 0.01	0.39 ± 0.16	0.07 ± 0.08	0.27 ± 0.03
	rms	0.164	0.205	0.164	0.20	0.210
Sérsic light	a	-2.469 ± 0.004	-1.60 ± 0.02	-2.60 ± 0.08	-2.53 ± 0.004	-2.497 ± 0.003
	b	-0.08 ± 0.01	-0.90 ± 0.03	0.18 ± 0.20	-0.04 ± 0.02	-0.01 ± 0.01
	c	-0.09 ± 0.01	0.2 ± 0.01	-0.06 ± 0.12	0.14 ± 0.04	-0.04 ± 0.02
	rms	0.114	0.032	0.126	0.122	0.126

law, with steepest α values being found for $n \sim 4$ and the smallest R_e .

5.2 Comparison of different DM models

We discuss here how different assumptions on the DM component affects the trends of the mass density slope. As shown in Figs. 2 and 3, the slope values are degenerate with halo model (see also best fits in Tables 1, 2 and 3). For most correlations, the Burkert and “high-concentration” NFW models (see blue and green curves) provide slope values encompassing the whole range of values for α_1 , with the reference NFW model being in between these models (Cardone & Tortora 2010; Cardone et al. 2011b). Notice that the estimate of total mass density slope is deeply related to the best-fitting Υ_\star , as for increasing Υ_\star the mass budget in the central regions resembles more the one for the light component alone. In fact, contracted halo models, which imply a larger DM content towards the galaxy center, with smaller Υ_\star (see Fig. 1), tend to give shallower slopes than the reference NFW models, with this behavior being even more pronounced for “high-concentration” models. On the other hand, Burkert profiles provide steeper slopes, in between those for NFW models and stellar mass density (i.e. constant- M/L) slopes (Tortora et al. 2013). Remarkably, in the case of Burkert models, the slopes show almost constant trends with all galaxy properties, including mass and radius, in sharp contrast with the significant trends obtained for all other models. In particular, the results for the model with $r_B = 1$ kpc closely resemble the slopes of the stellar mass distribution.

Notice that, different than for NFW models, we have not adopted a trend of core radius with galaxy mass (equivalent to an $M_{\text{vir}}-M_\star$ relation) for Burkert models, but just two reference values of $r_B = 1$ and 20 kpc. These values approximately bracket the results found for two elliptical galaxies by MSB11 and the range of core radii obtained by Thomas et al. (2009) using cored logarithmic haloes, which resemble Burkert profiles in the galactic centers. Thus, using a radius-mass relation would not change significantly our results for the Burkert profiles.

Notice that NFW models with fixed virial mass and concentration (red curves in the Figures) give shallower slopes than, but similar trends to, the NFW case. In some cases, the slopes are also (marginally) shallower than those for NFW contracted profiles. For “high-concentration” models, the trends deviate significantly – with higher (i.e. shallower) α values – from our reference model. This is more pronounced at low- relative to high-mass, making the trends of α with mass significantly shallower than for reference models. On the other hand, the trends with radius and σ_e are more robust to the $c_{\text{vir}}-M_{\text{vir}}$ prescription, in particular for $\alpha_1(R_e/2)$.

In summary, we find that the strong increase of the mass density slope with galaxy radius, as well as the decrease with σ_e , are robust findings against different ingredients of NFW halo models. The trend with mass is less robust, in that it is significantly shallower for “high-concentration” models. However, as noticed in Sec. 4, the “high-concentration” models provide overly low IMF normalizations at low galaxy mass (i.e. lower than those measured for a Chabrier IMF),

which might favour (somewhat) lower concentration profiles. Moreover, one can notice that the $c_{\text{vir}}-M_{\text{vir}}$ relation from LFS12 is derived by assuming a fixed Chabrier IMF. Although this might be important at high galaxy mass, where the IMF normalization is found to be larger than the Chabrier one (e.g. Tortora et al. 2013, and Fig. 1), we find fair agreement, at high radius/large mass, between density slopes for fiducial NFW and “high-concentration” models. In contrast, all correlations tend to be washed out when using Burkert profiles. However, such models, while reproducing quite well the dynamics of dwarf galaxies and spirals, likely provide too *light* haloes in massive ETGs (Cardone & Tortora 2010), with respect to many results pointing to a significant amount of DM at the virial radius in these systems (e.g., Benson et al. 2000; Marinoni & Hudson 2002; van den Bosch et al. 2007; Moster et al. 2010). Therefore, while we have included here also Burkert models in the analysis, these should be considered as rather unlikely for the most massive galaxies in our samples.

5.3 Impact of different assumptions

Our dynamical approach relies on several assumptions, i.e. (i) spherical symmetry, (ii) isotropy, (iii) no stellar M/L -gradients within a galaxy, and (iv) no significant rotation. We have performed a variety of tests, showing that these assumptions do not affect significantly the correlations of mass density slope with galaxy properties.

(i) In general, for a flattened system, the use of spherical models tends to over- (under-) estimate the inferred galaxy mass, if the system is seen edge-on (face-on). To minimize the fraction of non-spherical systems (e.g. S0’s), for both SPIDER and ATLAS^{3D} samples, we have restricted the analysis to “round” objects, with axis ratio $q > 0.8$. We found that the slope trends remain unchanged, within a few percent, with respect to those for the entire samples.

ii) To explore the effect of radial anisotropy, we have adopted two empirically motivated values of the radial anisotropy parameter, $\beta = +0.1$ and $+0.2$, respectively (Gerhard et al. 2001). For $\beta > 0$, the model velocity dispersion at a given radius is larger than for $\beta = 0$, with the net effect of reducing our inferred masses within that radius. For $\beta = +0.1$ and $+0.2$, the inferred masses at $1 R_e$ were found to change by ~ 2 and 4% , respectively, with negligible impact on the mass density slopes, considering the observed scatter of slope values.

iii) Radial gradients of M/L can also affect our density slope estimates. However, at optical wavebands, such gradients are very mild in massive ETGs (Tortora et al. 2011), and are expected to be even smaller in the NIR, where most of the integrated light from a stellar population is dominated by its old quiescent component. Indeed, the fact that for r-(ATLAS^{3D}) and K-(SPIDER)band data, we find consistent slope estimates, indicates that M/L gradients are not important for our analysis.

iv) The ATLAS^{3D} sample gives us the opportunity to test the impact of neglecting rotational velocity and galaxy flattening in our analysis. From best-fitting JAM models, the ATLAS^{3D} team obtained the best-fitting relation $V_{\text{circ}}^{\text{obs}}(R_{e,\text{maj}}) \approx 1.51 \times \sigma_e$, where V_{circ} is the model circular velocity and $R_{e,\text{maj}}$ is the effective radius along the galaxy

major axis (Cappellari et al. 2013b). Using the expression $V_{\text{circ}}^{\text{theo}} \equiv \sqrt{GM_{\text{dyn}}/r}$ we have converted the $V_{\text{circ}}^{\text{obs}}(R_{e,\text{maj}})$ from ATLAS^{3D} to a dynamical mass, M_{dyn} . Even in this case, we found that neglecting rotation has negligible effects, within a few percent, on the mass density slopes.

6 COMPARISON WITH LITERATURE

6.1 Observations

Fig. 5 compares some of our findings with independent estimates of the mass density slope from the literature. At the highest mass scales probed in the present work, our results are consistent with Auger et al. (2010), who fitted a sample of SLACS lenses, at intermediate redshifts, with a power-law mass density profile, $\rho(r) \propto r^\alpha$, combining gravitational lensing and central dynamics to probe the total mass distribution at $R_e/2$. They found the mass distribution to be well described by an isothermal profile (Treu & Koopmans 2004; Gavazzi et al. 2007; Auger et al. 2010). The average slope value from Auger et al. (2010) is plotted in the top panels of Fig. 5 (see red squares and error bars), vs. M_\star (left) and $f_{\text{DM}}(R_e/2)$ (right), respectively. Notice that Auger et al. (2010) derived stellar masses by assuming a Salpeter IMF. Therefore, to perform a meaningful comparison, we also converted our Chabrier-IMF M_\star ’s into Salpeter-IMF stellar masses, accounting for the different overall normalizations of the Chabrier and Salpeter IMFs.

The agreement between Auger et al. (2010) – who estimated the density slope of massive early-type lenses – and our most massive bin for fiducial NFW models, is excellent, with a good agreement also with respect to f_{DM} . The best fitted relation $\alpha_1(R_e/2)-M_\star^{\text{Chab}}$ shown in Table 1, because of the change of IMF, is now $\alpha_1(R_e/2) = -2.28 + 0.40x + 0.40x^2$, with $x = M_\star^{\text{Salp}}$ and a scatter of $rms = 0.255$. The trend with f_{DM} is best fitted by the polynomial $\alpha_1(R_e/2) = -2.49 + 2.86x - 1.91x^2$, with $x = f_{\text{DM}}(R_e/2)$ and a scatter of $rms = 0.130$.

However, Auger et al. (2010) assumed a fixed, Salpeter, IMF, while our dynamical approach leaves the IMF normalization – through the best-fitting stellar mass-to-light ratio – as a free model parameter. To test the effect of IMF normalization, we have selected only galaxies in our sample that are best described by a Salpeter-like normalization (with $1.6 < \delta_{\text{IMF}} < 2$). This selection leads to mild variations ($< 10\%$) in the slope trends at high galaxy mass (see purple curves in the Figure), with slopes still in excellent agreement with SLACS. The agreement is good also when we compare the trends with R_e and velocity dispersion with ours in the top panels in Fig. 2, as Auger et al. (2010) find shallower slopes at larger R_e and an almost constant trend with velocity dispersion.

Fig. 5 also shows that Burkert profiles (dashed and solid blue curves in the top panels) give slopes that are too steep (at the 2.5σ level) with respect to SLACS. Thus, the comparison of our dynamical analysis with gravitational lensing results at intermediate redshift seems to reject Burkert profiles as plausible models to describe the DM component of (massive) ETGs, while it is fully consistent with massive ETGs having an isothermal total mass density profile.

In the bottom panels of Fig. 5 we compare our findings,

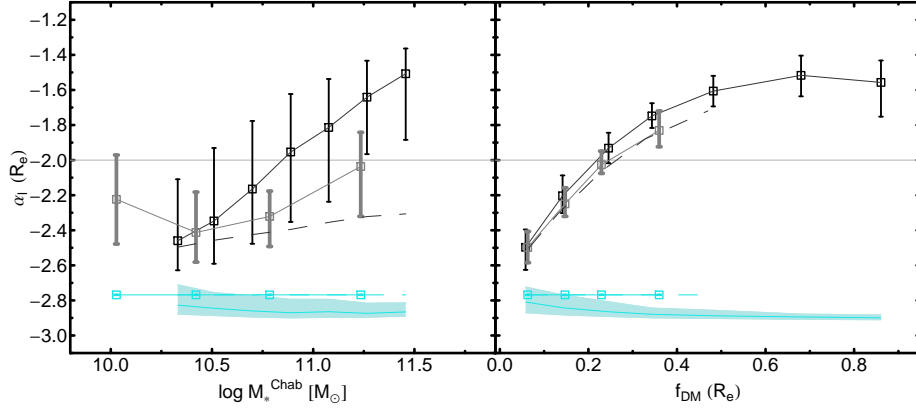


Figure 4. Comparison of trends of mass density slope, $\alpha_1(R_e)$, with M_* (left) and DM fraction, $f_{\text{DM}}(R_e)$ (right), between SPIDER (black squares) and ATLAS^{3D} (gray squares) samples. Error bars mark the 16-84th percentile scatter intervals on the slopes. Cyan shaded regions and squares mark the stellar mass slopes, at one R_e , for SPIDER and ATLAS^{3D}, respectively. Notice that for ATLAS^{3D}, the slope of the light distribution is constant, as the light profile is parameterized by a (fixed-shape) de Vaucouleurs model. As a comparison, we also plot, as dashed curves, the trends obtained for SPIDER ETGs when using SDSS-DR6 r-band de Vaucouleurs (rather than K-band Sérsic) models to parameterize the galaxy light profiles (dashed lines).

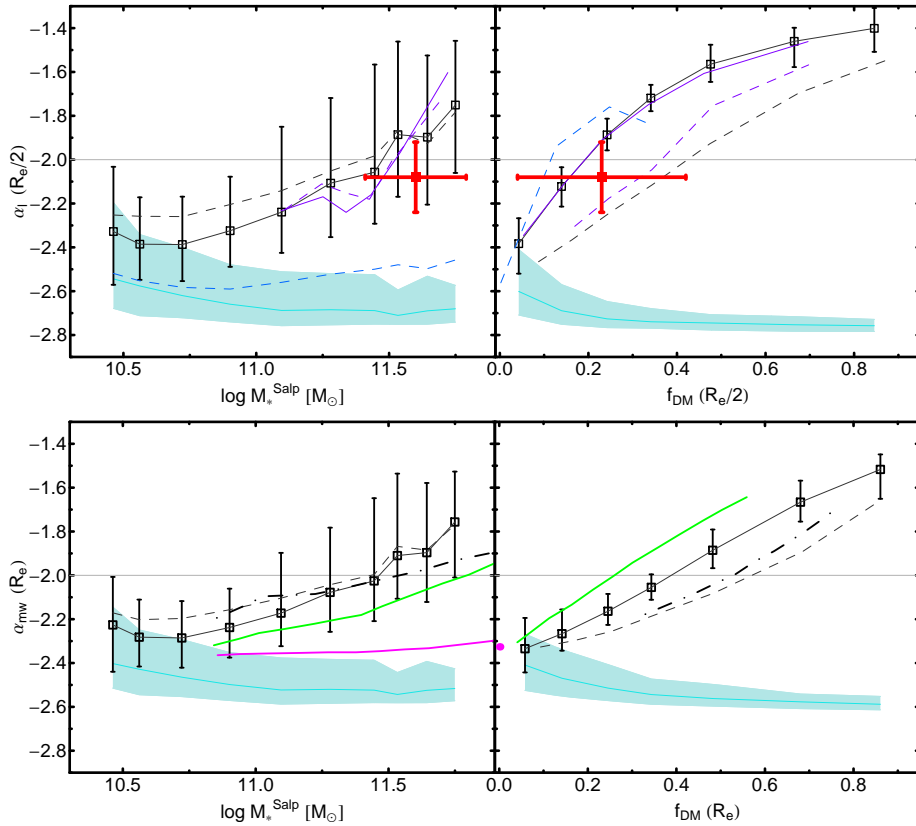


Figure 5. Comparison of total mass density profile slopes with data from the literature, as a function of M_* (left panels) and f_{DM} (right panels). Black symbols with error bars and cyan lines and regions are the same as in Figs. 2 and 3, plotting the slope trends of SPIDER ETGs, for our fiducial, NFW+Sérsic, model (black curve and error bars) and the slopes for the stellar mass profile only (cyan curve and shaded region), respectively. Top and bottom panels are for $\alpha_1(R_e/2)$ and $\alpha_{\text{mw}}(R_e)$, respectively. Literature data include: average slope and 1σ scatter for SLACS lenses (Auger et al. 2010), plotted with red squares and error bars in the top panels; slopes obtained for constant- M/L (magenta curves), NFW (green curves) and contracted-NFW (dot-dashed black curves) profiles from Dutton & Treu (2014) in the bottom panels. Purple solid and dashed lines in the top panels are the slope trends for SPIDER ETGs with Salpeter IMF normalization (see the text for details).

in terms of $\alpha_{\text{mw}}(R_e)$, with the dynamical analysis performed for a SDSS sample of ETGs, by Dutton & Treu (2014, hereafter DT14). The $\alpha_{\text{mw}}(R_e)$ is plotted vs. M_* (left) and $f_{\text{DM}}(R_e)$ (right). The best fitted relation $\alpha_1(R_e/2)-M_*^{\text{Salp}}$ is $\alpha_{\text{mw}}(R_e) = -2.21 + 0.31x + 0.38x^2$, with $x = M_*^{\text{Salp}}$ and a scatter of $rms = 0.196$. The trend with f_{DM} is best fitted by the polynomial $\alpha_{\text{mw}}(R_e) = -2.41 + 1.06x - 0.01x^2$, with $x = f_{\text{DM}}(R_e)$ and a scatter of $rms = 0.095$. The authors modelled the galaxy light profiles with the combination of an $n = 1$ and an $n = 4$ Sérsic law, with a suite of models to describe the DM distribution (including fiducial NFW, constant- M/L , contracted, and expanded models), with varying stellar M/L . The Figure compares their findings with ours, for NFW, contracted-NFW, and constant- M/L profiles. In general, the shape of the correlations are similar when comparing ours and DT14 results, but some offsets, at the 10% level, exist. In particular, constant- M/L models from DT14 (magenta curves) have slopes $\sim 8\%$ shallower than ours (cyan curve and shaded region), while mass density slopes for NFW models are steeper (shallower) than ours when plotted with respect to M_* (f_{DM}). A good agreement is found for contracted-NFW models. The offset between our NFW-model slopes and those of DT14 is likely due to the different modeling of the galaxy light distribution between our study and theirs. In fact, as shown in Fig. 3, the $\alpha_{\text{mw}}(R_e)$ of SPIDER ETGs with $n \sim 4$ is lower (i.e. steeper) than that for both higher- and lower- n galaxies, especially for NFW-model slopes, suggesting that a combination of $n = 1$ and $n = 4$ Sérsic laws, to model the light distribution of ETGs, can produce lower (steeper) $\alpha_{\text{mw}}(R_e)$ slopes than those for a single Sérsic law with variable n , consistent with what seen in the comparison of DT14 and our trends. A good agreement is found for the trend with R_e , while DT14 find shallower slopes in high- σ_* galaxies, in agreement with recent findings from gravitational lenses (Shu et al. 2014), but in contrast with our constant trends (see Fig. 3).

The fact that the mass density slope becomes shallower at high-, relative to low-, mass is also consistent with the findings of Humphrey & Buote (2010, hereafter HB10). Using *Chandra* X-ray data, under the assumption of hydrostatic equilibrium, HB10 analyzed a sample of 10 systems, spanning ~ 2 orders of magnitude in M_{vir} , from massive galaxies to clusters of galaxies, in the radial range from $\lesssim R_e$ to several R_e 's. They found isothermal profiles for galaxies, consistent with our results for massive ETGs, and shallower than isothermal slopes (up to $\alpha = -1.2$) for galaxy clusters.

6.2 Simulations

We compare our results with predictions for a suite of simulated galaxies, from Remus et al. (2013, hereafter R13). The comparison is shown in Fig. 6, where we plot mass density slopes, for our fiducial (NFW+Sérsic) model, as a function of stellar mass (left) and central DM fraction (right). R13 computed mass density slopes by fitting mass density profiles with a power-law, in the radial range $0.3 - 4 r_{1/2}$, where $r_{1/2}$ is the half-mass radius of a simulated galaxy. To perform a meaningful comparison, we re-computed our slopes with the same definition as in R13, converting the projected effective radius of a given galaxy into its half-mass (de-projected) radius. We used the relation $R_e = r_{1/2}/1.35$, which turns out to be independent of the Sérsic n (see, e.g., appendix B of

Wolf et al. 2010). We refer to the slopes, defined as in R13, as α_{av} .

Fig. 6 plots the α_{av} for all models from R13 (see dots with different colours), except for simulated BCGs, whose mass range is above that covered by our trends. The simulations include several high-resolution “binary mergers”, i.e. a) spiral-spiral mergers with a progenitor mass ratio 1 : 1 (black), b) spiral-spiral mergers with mass ratio 3 : 1 (blue), c) a mixed merger of a spiral galaxy with an elliptical, the latter formed by a 3:1 spiral-spiral merger (cyan), d) one spiral-spiral merger, with a mass ratio 3 : 1, and a large gas fraction of 80% (pink). Furthermore, we plot 17 simulated elliptical galaxies formed from multiple mergers, in the framework of a cosmological simulation: e) the most massive merger remnants, re-simulated with twice the spatial resolution of the original DM box (light-green), f) the less massive remnants, re-simulated with four times the original resolution of DM particles (dark-green), and g) four companion ellipticals, which are substructures within larger haloes (yellow). R13 referred to simulations (e–f) as CosmoZoom Ellipticals, and simulations (g) as CosmoZoom Companions. All simulations have been performed by R13 with modified versions of the parallel TreePM-SPH-code GADGET-2, including the effect of star formation and feedback from SNe's, assuming a Salpeter IMF. Black hole (BH) growth and feedback are included in the binary merger simulations only, while CosmoZoom simulations do not include any BH treatment.

Several simulated galaxies (in particular the most massive CosmoZoom Ellipticals) have masses larger than the range covered by our data, hampering a direct comparison to our results. Therefore, we focus the comparison on objects having $\log M_* \lesssim 11.8$ in Fig. 6. All binary mergers in this mass range are in good agreement with our results in both the $\alpha_{\text{av}}-M_*$ and $\alpha_{\text{av}}-f_{\text{DM}}$ plots. The same result holds when comparing simulations to the trends for ETGs with a Salpeter-like IMF normalization (see Sec. 6), i.e. the same IMF as in R13. On the contrary, CosmoZoom galaxies, in the mass range from $\log M_* \sim 11.3$ to $\log M_* \sim 11.8$ (green and yellow dots in the Figure) have systematically steeper slopes, at a given stellar mass, than our data, which is more consistent with slopes for a constant M/L profile (i.e. the cyan region in the Figure). A similar discrepancy exists with respect to f_{DM} , although in the $\alpha_{\text{av}}-f_{\text{DM}}$ plane, the deviation of CosmoZoom galaxies from our fiducial trends (black curves) is smaller than in the $\alpha_{\text{av}}-M_*$ diagram. This is due to the fact that, at fixed stellar mass, CosmoZoom galaxies also have lower DM fractions than real galaxies.

We argue that the excellent agreement found between our results and the predictions of binary merger simulations can be due to the inclusion of BH feedback in them, which is more efficient than SN-feedback in suppressing star formation (Tortora et al. 2009a; Martizzi et al. 2014), producing less stellar mass in the galaxy centre, and nearly isothermal total mass profiles, in agreement with the observed trends.

Although the CosmoZoom simulations are offset with respect to the observed trends in the $\alpha_{\text{av}}-M_*$ diagram, they exhibit a similar trend as in the data, with mass density slope increasing (becoming shallower) with galaxy mass. The existence of such trend can be explained by a smaller amount of dissipation during the formation of high-, relative to low-, mass galaxies. During a merger, gas dissipates

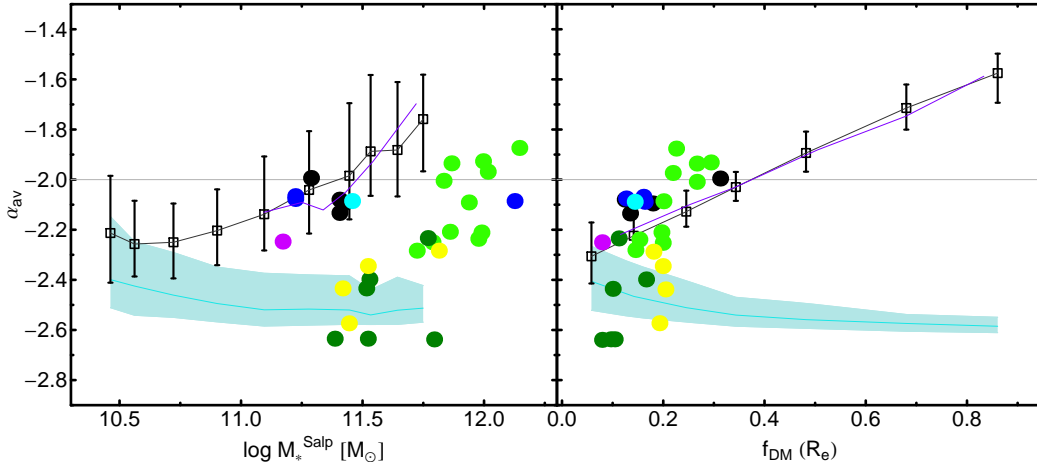


Figure 6. Comparison of total mass density slope trends with predictions for simulated galaxies from R13. Left and right panels plot α_{av} vs. M_* and f_{DM} (within $1 R_e$), respectively. The slope, α_{av} , is defined by fitting mass density profiles with a power-law, in the radial range $0.3 - 4 r_{1/2}$, where $r_{1/2}$ is the galaxy half-mass radius (i.e. adopting the same slope definition as in R13, see the text for details). Black symbols with error bars and cyan lines and regions are the same as in Figs. 2 and 3. Our stellar masses are re-scaled to a Salpeter IMF, as in R13. Purple lines are the observed trends for the subsample of SPIDER ETGs with Salpeter-like IMF normalization (see Sec. 6.1). Dots with different colours are simulated galaxies from R13: black, blue, cyan and pink dots correspond to idealized single binary mergers, while light-green, dark-green, and yellow dots are for mergings systems drawn from cosmological simulations (see Sec. 6.2 for details). Notice the good agreement of our trends with binary mergers simulations, including also the effect of BH growth and feedback.

its kinetic energy, falling into the galaxy center and forming new stars. Therefore, a higher level of dissipation leads to a more prominent contribution from newly formed stars to the total mass density in the center, steepening the total density slope, as observed in low- relative to high-mass (both observed and simulated) ETGs. The existence of a strong correlation between density slope and radius (Section 5) also supports this interpretation, as dissipation would favour the formation of a smaller size system.

7 SUMMARY AND CONCLUSIONS

In the present work, we have analyzed the stellar and DM distribution in the central regions of ETGs, using a large sample of nearby galaxies from the SPIDER sample (La Barbera et al. 2010), as well as a complementary dataset of ATLAS^{3D} ETGs (Cappellari et al. 2011). We have compared our findings to independent results from the literature, and predictions from numerical simulations. We have modeled each galaxy with two components, a Sérsic (de Vaucouleurs) profile for the SPIDER (ATLAS^{3D}) sample plus a variety of viable profiles for the DM distribution. Our reference model is based on an NFW (DM) plus a Sérsic (stars) component, assuming a concentration–virial mass relation from simulations (Macciò et al. 2008) and the virial to stellar mass relation of Moster et al. (2010). Assuming circular symmetry, no rotation, and neglecting radial gradients of the stellar mass-to-light ratio, Υ_* , in ETGs, we derive the only free parameter of the model, the Υ_* , from the central velocity dispersion, σ_{Ap} and σ_e , of each galaxy. None of these assumptions is found to affect significantly our results. From the two-component models, we derive the total mass density slope in the central regions of ETGs, and analyze its correlation with several galaxy parameters, i.e. σ_e , M_* ,

R_e , and n . Our analysis (i) extends, with an independent approach, down to $M_* \sim 10^{10} M_\odot$, the results of gravitational lensing studies of massive galaxies (Bolton et al. 2006; Bolton et al. 2008; Auger et al. 2009; Auger et al. 2010); (ii) complements previous work (e.g. Humphrey & Buote 2010; Dutton & Treu 2014; Chae et al. 2014; Oguri et al. 2014) by targeting two independent, large, samples of ETGs, and using a better tracer (the K-band light) of the stellar mass distribution in galaxies; and (iii) investigates the impact of a variety of modeling ingredients on the inferred Υ_* and central mass density slopes.

Our results can be summarized as follows:

- Consistent with our previous work (Tortora et al. 2013), we find that ETGs at high σ_e have larger Υ_* than that expected for a Chabrier IMF when fitting either colours or galaxy spectra with stellar population models, i.e. that the mismatch parameter, $\delta_{\text{IMF}} = \Upsilon_*/\Upsilon_*^{\text{Chab}}$, becomes significantly larger than one at high σ_e . This result can be interpreted as a systematic variation of the IMF normalization (i.e. the amount of stellar mass in the IMF) with σ_e . In the present work, we find that δ_{IMF} also increases with stellar mass and R_e (but to less extent than the trend with σ_e), while it decreases with the Sérsic n . Using ATLAS^{3D} sample we find, on average, larger Υ_* and shallower correlations with all the parameters. These results are consistent with studies of gravity-sensitive features in ETGs, finding that the IMF becomes bottom-heavier than a “standard”, MW-like, distribution in high-, relative to low- σ_e ETGs (e.g. Ferreras et al. 2013; La Barbera et al. 2013; Spiniello et al. 2014). At low σ_e ($\sim 100 \text{ km s}^{-1}$), the value of δ_{IMF} (~ 1) implies a MW-like IMF normalization, consistent with results for late-type galaxies (Sonnenfeld et al. 2012; Brewer et al. 2012), and the combined lensing and stellar population analysis of Ferreras et al. (2008, 2010).

The trends of δ_{IMF} hold for all DM profiles explored in this work, with lower δ_{IMF} 's for contracted halo and “high-concentration” models (the latter being based on the $c_{\text{vir}} - M_{\text{vir}}$ relation from LFS12).

– For our reference model (see above), the total mass density slope in the centre of ETGs increases (becoming less negative) with galaxy mass and galaxy size. For the ATLAS^{3D} sample we find consistent results to those for SPIDER ETGs, although the trend with mass is steeper for the latter. In more detail, we find that low-mass (small) ETGs have slopes consistent with those for constant- M/L profiles, while massive (large R_e) systems have a nearly isothermal density slope ($= -2$), consistent with gravitational lensing results (e.g., Gavazzi et al. 2007; Auger et al. 2010). The trends of mass density slope are consistent with independent results from the literature (Humphrey & Buote 2010; Dutton & Treu 2014). In terms of central velocity dispersion, the density slope decreases with central velocity dispersion (but to less extent than the amount of variation with R_e), while it exhibits a double-value behaviour with the Sérsic n , increasing at both low and high n , with a minimum for n between 3 and 5 (depending on the method to compute the slope).

– The trends of mass density slope are the same for NFW and contracted-NFW models, and do not change when assuming a fixed virial mass (and concentration) for all galaxies (rather than a virial to stellar mass relation, such as that of Macciò et al. 2008). When adopting a Burkert profile, the slope tends to be more constant as a function of all galaxy parameters explored. However, for the most massive ETGs, the “light” haloes described by Burkert models seem to be rejected by lensing results (Auger et al. 2009; see also Cardone & Tortora 2010).

– Using a $c_{\text{vir}} - M_{\text{vir}}$ relation from observations (LFS12) rather than simulations (Macciò et al. 2008) affects significantly some trends of density slope with galaxy parameters. In particular, while the slope keeps increasing with galaxy radius also for “high-concentration” models (with $c_{\text{vir}} - M_{\text{vir}}$ from LFS12), the trends with mass become flatter in this case. On the other hand, the trends with central velocity dispersion are the same for all models.

Our results corroborate a picture whereby the total mass density profile in the central regions of ETGs is “non-homologous”, approaching a constant- M/L distribution at low mass – where stars dominate the total mass budget in the center –, and an isothermal profile in the most massive ETGs, whose central regions are more DM dominated. The fact that the mass density slope of groups and clusters of galaxies seems to be shallower than that of massive galaxies (e.g. Sand et al. 2008; Humphrey & Buote 2010) further supports the “non-homology” of the total mass distribution of galactic systems.

To understand the implications of our findings in the framework of galaxy assembly, we have also compared our results, i.e. the trends of total mass density slope, with simulation predictions from R13. The comparison indicates that BH growth and feedback are essential ingredients during the formation of ETGs, as only simulations including them are able to reproduce the mass density slope, DM fraction, and stellar mass we have measured in the central regions of ETGs. Also, we find that both observations and simu-

lations predict an increase of the total mass density slope with galaxy mass. We argue that this trend is because gas dissipation has been more important during the formation of low-, relative to high-, mass galaxies. In such a picture, a steep profile is due to the formation of new stars inwards, as the gas, dissipating its kinetic energy, falls into the galaxy central regions, while gas-poor mergers tend to make the slopes isothermal.

The present work shows that observations and simulations are now converging to provide a consistent characterization of the luminous and DM components in the central regions of ETGs. Nevertheless, important questions remain still open, like the discrepancy between halo concentration and mass from N-body simulations, and those obtained from lensing studies. In the future, it will be important to extend our results to the outermost regions of these galaxies, taking advantage of data covering a wide galactocentric baseline (e.g. kinematical tracers as planetary nebulae or globular clusters, Romanowsky et al. 2009; Napolitano et al. 2009; Napolitano et al. 2011; Pota et al. 2013) and accounting for radial gradients of the stellar IMF (Martín-Navarro et al. 2014; Pastorello et al. 2014). From the theoretical viewpoint, it will be also interesting to explore phenomenologically-motivated models for the mass distribution in galaxies (e.g. Zhao 1997; Tortora et al. 2007; Cardone et al. 2009), as well as alternative theories with modified gravity, like MOND (Milgrom 1983b,a; Cardone et al. 2011a; Tortora et al. 2014) and modifications of the Einstein theory (e.g. $f(R)$, Lubini et al. 2011; Napolitano et al. 2012).

ACKNOWLEDGMENTS

We thank the referee for the kind report. CT has received funding from the European Union Seventh Framework Programme (FP7/2007-2013) under grant agreement n. 267251.

REFERENCES

- Auger M. W., Treu T., Bolton A. S., Gavazzi R., Koopmans L. V. E., Marshall P. J., Bundy K., Moustakas L. A., 2009, *ApJ*, 705, 1099
- Auger M. W., Treu T., Bolton A. S., Gavazzi R., Koopmans L. V. E., Marshall P. J., Moustakas L. A., Burles S., 2010, *ApJ*, 724, 511
- Benson A. J., Cole S., Frenk C. S., Baugh C. M., Lacey C. G., 2000, *MNRAS*, 311, 793
- Blumenthal G. R., Faber S. M., Flores R., Primack J. R., 1986, *ApJ*, 301, 27
- Bolton A. S., Burles S., Koopmans L. V. E., Treu T., Gavazzi R., Moustakas L. A., Wayth R., Schlegel D. J., 2008, *ApJ*, 682, 964
- Bolton A. S., Burles S., Koopmans L. V. E., Treu T., Moustakas L. A., 2006, *ApJ*, 638, 703
- Brewer B. J. et al., 2012, *MNRAS*, 422, 3574
- Bruzual G., Charlot S., 2003, *MNRAS*, 344, 1000
- Buote D. A., Gastaldello F., Humphrey P. J., Zappacosta L., Bullock J. S., Brighenti F., Mathews W. G., 2007, *ApJ*, 664, 123
- Burkert A., 1995, *ApJ*, 447, L25

- Cappellari M. et al., 2006, *MNRAS*, 366, 1126
 Cappellari M. et al., 2011, *MNRAS*, 413, 813
 Cappellari M. et al., 2012, *Nature*, 484, 485
 Cappellari M. et al., 2013a, *MNRAS*, 432, 1862
 Cappellari M. et al., 2013b, *MNRAS*, 432, 1709
 Cardone V. F., Angus G., Diaferio A., Tortora C., Molinaro R., 2011a, *MNRAS*, 412, 2617
 Cardone V. F., Del Popolo A., Tortora C., Napolitano N. R., 2011b, *MNRAS*, 416, 1822
 Cardone V. F., Tortora C., 2010, *MNRAS*, 409, 1570
 Cardone V. F., Tortora C., Molinaro R., Salzano V., 2009, *A&A*, 504, 769
 Chabrier G., 2001, *ApJ*, 554, 1274
 Chae K.-H., Bernardi M., Kravtsov A. V., 2014, *MNRAS*, 437, 3670
 Ciotti L., 1991, *A&A*, 249, 99
 Conroy C., van Dokkum P. G., 2012, *ApJ*, 760, 71
 de Blok W. J. G., McGaugh S. S., Bosma A., Rubin V. C., 2001, *ApJ*, 552, L23
 de Vaucouleurs G., 1948, *Annales d'Astrophysique*, 11, 247
 Del Popolo A., 2009, *ApJ*, 698, 2093
 Dutton A. A. et al., 2011, *MNRAS*, 416, 322
 Dutton A. A., Macciò A. V., Mendel J. T., Simard L., 2013, *MNRAS*, 432, 2496
 Dutton A. A., Mendel J. T., Simard L., 2012, *MNRAS*, 422, L33
 Dutton A. A., Treu T., 2014, *MNRAS*, 438, 3594 (DT14)
 Ferreras I., La Barbera F., de la Rosa I. G., Vazdekis A., de Carvalho R. R., Falcón-Barroso J., Ricciardelli E., 2013, *MNRAS*, 429, L15
 Ferreras I., Saha P., Burles S., 2008, *MNRAS*, 383, 857
 Ferreras I., Saha P., Leier D., Courbin F., Falco E. E., 2010, *MNRAS*, 409, L30
 Gavazzi R., Treu T., Rhodes J. D., Koopmans L. V. E., Bolton A. S., Burles S., Massey R. J., Moustakas L. A., 2007, *ApJ*, 667, 176
 Gerhard O., Kronawitter A., Saglia R. P., Bender R., 2001, *AJ*, 121, 1936
 Gnedin O. Y., Kravtsov A. V., Klypin A. A., Nagai D., 2004, *ApJ*, 616, 16
 Goudfrooij P., Kruijssen J. M. D., 2013, *ApJ*, 762, 107
 Goudfrooij P., Kruijssen J. M. D., 2014, *ApJ*, 780, 43
 Humphrey P. J., Buote D. A., 2010, *MNRAS*, 403, 2143 (HB10)
 Koopmans L. V. E. et al., 2009, *ApJ*, 703, L51
 La Barbera F., de Carvalho R. R., de La Rosa I. G., Lopes P. A. A., Kohl-Moreira J. L., Capelato H. V., 2010, *MNRAS*, 408, 1313
 La Barbera F., de Carvalho R. R., Kohl-Moreira J. L., Gal R. R., Soares-Santos M., Capaccioli M., Santos R., Sant'anna N., 2008, *PASP*, 120, 681
 La Barbera F., Ferreras I., Vazdekis A., de la Rosa I. G., de Carvalho R. R., Trevisan M., Falcón-Barroso J., Ricciardelli E., 2013, *MNRAS*, 433, 3017
 Leier D., Ferreras I., Saha P., 2012, *MNRAS*, 424, 104 (LFS12)
 Lubini M., Tortora C., Näf J., Jetzer P., Capozziello S., 2011, *European Physical Journal C*, 71, 1834
 Macciò A. V., Dutton A. A., van den Bosch F. C., 2008, *MNRAS*, 391, 1940
 Marinoni C., Hudson M. J., 2002, *ApJ*, 569, 101
 Martín-Navarro I., La Barbera F., Vazdekis A., Falcón-Barroso J., Ferreras I., 2014, *ArXiv e-prints*
 Martizzi D., Teyssier R., Moore B., 2014, *ArXiv e-prints*
 Memola E., Salucci P., Babić A., 2011, *A&A*, 534, A50 (MSB11)
 Milgrom M., 1983a, *ApJ*, 270, 371
 Milgrom M., 1983b, *ApJ*, 270, 365
 Moore B., Governato F., Quinn T., Stadel J., Lake G., 1998, *ApJ*, 499, L5
 Moster B. P., Somerville R. S., Maulbetsch C., van den Bosch F. C., Macciò A. V., Naab T., Oser L., 2010, *ApJ*, 710, 903
 Napolitano N. R., Capozziello S., Romanowsky A. J., Capaccioli M., Tortora C., 2012, *ApJ*, 748, 87
 Napolitano N. R. et al., 2011, *MNRAS*, 411, 2035
 Napolitano N. R. et al., 2009, *MNRAS*, 393, 329
 Napolitano N. R., Romanowsky A. J., Tortora C., 2010, *MNRAS*, 405, 2351
 Navarro J. F., Frenk C. S., White S. D. M., 1996, *ApJ*, 462, 563
 Navarro J. F., Frenk C. S., White S. D. M., 1997, *ApJ*, 490, 493
 Oguri M., Rusu C. E., Falco E. E., 2014, *MNRAS*, 439, 2494
 Pastorello N., Forbes D. A., Foster C., Brodie J. P., Usher C., Romanowsky A. J., Strader J., Arnold J. A., 2014, *ArXiv e-prints*
 Pota V. et al., 2013, *MNRAS*, 428, 389
 Remus R.-S., Burkert A., Dolag K., Johansson P. H., Naab T., Oser L., Thomas J., 2013, *ApJ*, 766, 71 (R13)
 Romanowsky A. J., Strader J., Spitler L. R., Johnson R., Brodie J. P., Forbes D. A., Ponman T., 2009, *AJ*, 137, 4956
 Salpeter E. E., 1955, *ApJ*, 121, 161
 Salucci P., Burkert A., 2000, *ApJ*, 537, L9
 Sand D. J., Treu T., Ellis R. S., Smith G. P., Kneib J.-P., 2008, *ApJ*, 674, 711
 Shu Y. et al., 2014, *ArXiv e-prints*
 Sonnenfeld A., Treu T., Gavazzi R., Marshall P. J., Auger M. W., Suyu S. H., Koopmans L. V. E., Bolton A. S., 2012, *ApJ*, 752, 163
 Spiniello C., Trager S., Koopmans L. V. E., Conroy C., 2014, *MNRAS*, 438, 1483
 Spiniello C., Trager S. C., Koopmans L. V. E., Chen Y. P., 2012, *ApJ*, 753, L32
 Swindle R., Gal R. R., La Barbera F., de Carvalho R. R., 2011, *AJ*, 142, 118
 Thomas J., Saglia R. P., Bender R., Thomas D., Gebhardt K., Magorrian J., Corsini E. M., Wegner G., 2009, *ApJ*, 691, 770
 Thomas J. et al., 2011, *MNRAS*, 415, 545
 Tortora C., Antonuccio-Delogu V., Kaviraj S., Silk J., Romeo A. D., Becciani U., 2009a, *MNRAS*, 396, 61
 Tortora C., Cardone V. F., Piedipalumbo E., 2007, *A&A*, 463, 105
 Tortora C., La Barbera F., Napolitano N. R., de Carvalho R. R., Romanowsky A. J., 2012, *MNRAS*, 425, 577
 Tortora C., Napolitano N. R., Romanowsky A. J., Capaccioli M., Covone G., 2009b, *MNRAS*, 396, 1132
 Tortora C., Napolitano N. R., Romanowsky A. J., Jetzer P., Cardone V. F., Capaccioli M., 2011, *MNRAS*, 418, 1557

- Tortora C., Romanowsky A. J., Cardone V. F., Napolitano N. R., Jetzer P., 2014, MNRAS, 438, L46
- Tortora C., Romanowsky A. J., Napolitano N. R., 2013, ApJ, 765, 8
- Treu T., Auger M. W., Koopmans L. V. E., Gavazzi R., Marshall P. J., Bolton A. S., 2010, ApJ, 709, 1195
- Treu T., Koopmans L. V. E., 2004, ApJ, 611, 739
- van den Bosch F. C. et al., 2007, MNRAS, 376, 841
- Vazdekis A., Ricciardelli E., Cenarro A. J., Rivero-González J. G., Díaz-García L. A., Falcón-Barroso J., 2012, MNRAS, 3156
- Wegner G. A., Corsini E. M., Thomas J., Saglia R. P., Bender R., Pu S. B., 2012, AJ, 144, 78
- Weidner C., Ferreras I., Vazdekis A., La Barbera F., 2013, MNRAS, 435, 2274
- Wolf J., Martinez G. D., Bullock J. S., Kaplinghat M., Geha M., Muñoz R. R., Simon J. D., Avedo F. F., 2010, MNRAS, 406, 1220
- Zhao H., 1997, MNRAS, 287, 525